ACS APPLIED NANO MATERIALS

www.acsanm.org Article

Electric Field Modulation on MoS_2 Nanoreactors for Enhanced Photodynamic Therapy of Severe Acute Pancreatitis

Ruixi Chu,[⊥] Yuansong Sun,[⊥] Jianhua Liu,[⊥] Yibin Du,[⊥] Weihong Chen,[⊥] Rongrong Gu, and Sheng Ye*

Cite This: *ACS Appl. Nano Mater.* 2025, 8, 3272−3280 Read Online

ACCESS | Metrics & More | Article Recommendations | Supporting Information

ABSTRACT: Severe acute pancreatitis (SAP) is one of the most common gastrointestinal emergencies in clinical practice. However, there are many limitations in clinical treatment, such as complicated processes with a long cycle and poor prognosis. As one of the emerging therapeutic methods in recent years, nanomaterial-mediated photodynamic therapy (PDT) has brought light to the treatment of disease. In this work, we design three morphologically controlled MoS_2 nanoreactors for SAP photodynamic therapy. The hollow MoS_2 (H-MoS_2) nanoreactor possesses the highest electric field intensity and light absorption, resulting in the best therapeutic effects under 808 nm of irradiation. The amylase and lipase were reduced to one-third of the SAP, and the apoptosis rate of pancreatic acinar cells was reduced to one-half of that in the SAP. Our work opens a window for the construction of high-performance nanomedicine for SAP photodynamic therapy, especially in more inflammatory diseases.

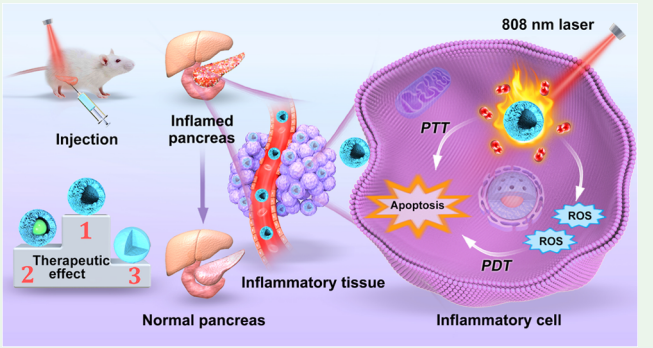

KEYWORDS: *severe acute pancreatitis, MoS_2, morphology, electric field, photodynamic therapy*

1. INTRODUCTION

Acute pancreatitis is one of the most common acute abdominal diseases in clinical practice, with a mortality rate of over 5% in confirmed patients.[1−3] Due to changes in dietary structure and lifestyle, its incidence is increasing year by year.[4] About 20% of them will progress to severe acute pancreatitis (SAP) that leads to multiple organ failure in the human body, including the lungs, liver, and kidneys and eventually death.[5−8] Commonly used modern clinical acute pancreatitis therapies, including fluid therapy, analgesia, nutritional support, and treatment for causes and complications, have several disadvantages, such as a complicated process with a long cycle and poor prognosis. Zheng et al. designed a hollow Prussian blue nanozyme (PBzyme) with a size of about 60 nm and a mesoporous surface with a large specific surface area. The study showed that PBzyme significantly reduced the levels of pro-inflammatory factors in the AP mouse model, and PBzyme may inhibit the expression of inflammatory genes through the TLRs/NF-κB signaling pathway.[9] However, the cyanide contained in its composition can cause potential toxicity. Photodynamic therapy (PDT), as a noninvasive therapeutic approach triggered by light, has recently attracted widespread interest.[10−12] It produces superoxide anion ($^{\bullet}O_2^-$), hydroxyl radical ($^{\bullet}OH$), and other types of reactive oxygen species (ROS) under light irradiation by utilizing nanomaterials to regulate the chemical environment in the body of diseased organisms, thus realizing the recovery of normal biological functions and achieves a therapeutic effect.

Molybdenum is one of the essential trace dietary elements for organism survival.[13] Some molybdenum-containing enzymes are involved in key metabolic activities such as xanthine oxidase, aldehyde oxidase, and sulfite oxidase.[14] The high safety of many molybdenum-based compounds has been effectively confirmed.[15−17] MoS_2 nanomaterials show low toxicity and good biocompatibility in vivo, and the surface is easy to modify, in addition, due to its unique band gap structure and quantum limiting effect, MoS_2 has efficient photothermal conversion ability in near-infrared (NIR) light.[18−22] In recent years, MoS_2 has received increasing attention as a photodynamic nanomaterial to treat various diseases and holds an important position in the field of nanomedicine.[23−28]

Herein, we designed and prepared three morphologically controlled MoS_2 nanoreactors for SAP photodynamic therapy. Compared with solid MoS_2 (S-MoS_2) and yolk−shell MoS_2 (Y-MoS_2), the hollow MoS_2 (H-MoS_2) nanoreactor has the highest electric field intensity and light absorption, resulting in a significant therapeutic effect. Under the excitation of light, the electrons in the valence band of MoS_2 jump into the conduction

Received: August 15, 2024
Revised: January 27, 2025
Accepted: January 31, 2025
Published: February 10, 2025

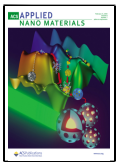

https://doi.org/10.1021/acsanm.4c04712
ACS Appl. Nano Mater. 2025, 8, 3272−3280

Scheme 1. Schematic Illustration of the Synthesis Process and Morphological Control of Three MoS_2 Nanoreactors for SAP Photodynamic Therapy

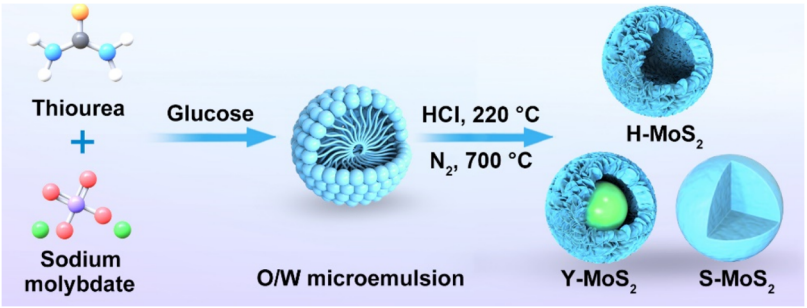

band, and the holes remain in the valence band, forming the electron-rich reducing end and the hole-rich oxidation end, which react with oxygen and water respectively to generate ROS, so as to achieve the purpose of treating SAP. Under the irradiation of 808 nm NIR, the amylase and lipase in the H-MoS_2 were reduced to one-third of the SAP, and the apoptosis rate of pancreatic acinar cells was reduced to half of that in the SAP.

2. EXPERIMENTAL PROCEDURE

2.1. Materials. Hexadecyltrimethylammonium bromide (CTAB) and sodium molybdate were purchased from MACKLIN (Shanghai, China). Ethylene glycol, thiourea, and D(+)-Glucose monohydrate were obtained from Sinopharm Chemical Reagent Co., Ltd. (Shanghai, China). Hydrochloric acid and *n*-butanol were purchased from XILONG (Guangdong, China). Annexin V-FITC/PI apoptosis kit was obtained from MULTISCIENCES (Zhejiang, China). Pancreatic fermentation was obtained from Beyotime Biotechnology (Shanghai, China). Phosphate buffer solution was purchased from HyClone (Logan, Utah). Dulbecco's modified Eagle's medium was brought from Cytiva (Washington, DC). All reagents used in this work were analytical reagents (AR) and were not used in any further purification cases.

2.2. Synthesis of MoS_2. In this paper, hollow MoS_2 (H-MoS_2), yolk−shell MoS_2 (Y-MoS_2), and solid MoS_2 (S-MoS_2) were successfully synthesized by a hydrothermal method of sodium molybdate in a mixed solution of hexadecyltrimethylammonium bromide and *n*-butanol. Normally, appropriate amounts of sodium molybdate and glucose were dissolved in pure water and then dropped into the mixed solution of CTAB and *n*-butanol at a rate of 2 s per drop. After stirring the above solution for 2 h, an additional 50 mL of ethylene glycol was added at a rate of one drop per second. After that, we can obtain three morphologies of molybdenum disulfide by adding different concentrations of hydrochloric acid. When the amount of hydrochloric acid is 0.3−0.5 mL, H-MoS_2 can be synthesized, 0.6−0.8 mL of hydrochloric acid can be obtained Y-MoS_2, and when the concentration of hydrochloric acid reaches 1.0 mL or more, S-MoS_2 existed stably. Finally, thiourea was added to provide a sulfur source. The resulting solution was transferred to a Teflon reactor for solvothermal treatment at 220 °C for 24 h. The samples were obtained after thoroughly washing with water and alcohol five times followed by vacuum drying at 60 °C until completely dry. The morphology becomes stronger after nitrogen calcination at 700 °C in a tube furnace (Anhui Kemi Machinery Technology Co., Ltd.).

2.3. Characterization. Transmission electron microscopy (TEM) and scanning electron microscopy (SEM) images were taken on an HT-7700 transmission electron microscope and a Hitachi S-4800 cold field emission scanning electron microscope, respectively. An ultraviolet−visible spectrophotometer (SHIMADZU, UV-2600i) was used to analyze the absorption of UV−visible light. Powder X-ray diffraction (XRD, X'Pert PRO MPD) analysis was performed using the Rigaku D/Max 2500 PC diffractometer (test range: 10−80°). Raman spectroscopies were conducted by using a wavelength of 532 nm on a Raman spectrometer (LabRAM HR Evolution, France). The measurements of the photocurrent response and electrochemical impedance spectroscopy (EIS) curves were performed at an electrochemical workstation (CS310M) and xenon lamp source (CEL-HXF300-T3). X-ray photoelectron spectroscopy (XPS) data were collected on a Thermo Scientific Escalab (ESCALAB 250Xi, Massachusetts) with a monochromatized Al Kα X-ray source. Characteristic absorption peak in the infrared spectrum was analyzed via Fourier transform infrared spectrometry (FT-IR). Electron paramagnetic resonance (EPR) data were collected by a Bruker A200 instrument.

2.4. Finite-Different Time-Domain Simulations (FDTD). We have employed FDTD to calculate the electric field distribution of MoS_2 in three surface morphologies. In the calculation process, we configured the *x*, *y*, and *z* directions to perfectly match the layer conditions to prevent unphysical scattering. We divided the region of calculation into a 0.5 nm × 0.5 nm × 0.5 nm mesh to obtain precise calculation results. Crucially, we adopt a total scattering field light source as the excitation source, which is incident perpendicular to the nanostructures along the *Z*-direction. Finally, we used an electric field monitor to obtain the electric field distribution of the nanostructures.

2.5. In Vitro Biocompatibility. To verify the biocompatibility of MoS_2, we selected mouse fibroblasts (L929) in vitro experiments. First, different concentrations of MoS_2 were placed on a 96-well culture plate, and the recovered L929 cells were seeded on the plate and incubated overnight at 37 °C. After 48 h, we replaced the old cell culture medium with a fresh RMPI1640 containing CCK-8 test solution. After incubation for 2 h, absorbance was measured to calculate the cell activity of each group. Moreover, we conducted in vitro hemolysis experiments using Sprague−Dawley (SD) rat red blood cells to evaluate the hemolysis rate of MoS_2. First, whole blood was obtained from healthy SD rats using the eyeball blood collection method, collected in an anticoagulant tube, shaken evenly, and centrifuged at 3000 rpm for 10 min to obtain red blood cells. Different concentrations of MoS_2 were prepared, and 1 mL of different concentrations of MoS_2, 1 mL of phosphate-buffered saline (PBS) solution, and 1 mL of ultrapure water were taken, and they were placed in an EP tube. 20 μL of red blood cells was added and incubated for 2 h. Finally, the hemolysis rate was calculated by measuring the absorbance value of the supernatant after centrifugation.

2.6. MoS_2 Treatment Alleviated Severe Acute Pancreatitis in Mice. Our animal experiments have been approved by the Animal Experiment Ethics Committee of the Second Affiliated Hospital of Anhui Medical University. Male SD rats weighing 240 ± 10 g, 3−4 months old, were obtained from the experimental center. All rats were randomly divided into 6 groups, including normal, SAP, MoS_2, H-MoS_2+NIR, Y-MoS_2+NIR, and S-MoS_2+NIR. All rats were fed adaptively for 1 week before the start of the experiment. After an intraperitoneal injection of pentobarbital (50 mg/kg), it was confirmed that all rats had entered an anesthetic state and maintained normal breathing and heartbeat with no significant abnormalities in vital signs. 20% arginine was injected into the abdominal cavity twice at a rate of 12.5 mL/500 g, with an interval of 1 h between each injection. 24 h after the completion of the SAP model, 1 mL of MoS_2 solution was injected intraperitoneally, and the control group was replaced with the same volume of physiological saline. After 24 h of injection of MoS_2 solution, all rats were exposed to the 808 nm light at the intensity of 275.52 J and

https://doi.org/10.1021/acsanm.4c04712
ACS Appl. Nano Mater. 2025, 8, 3272−3280

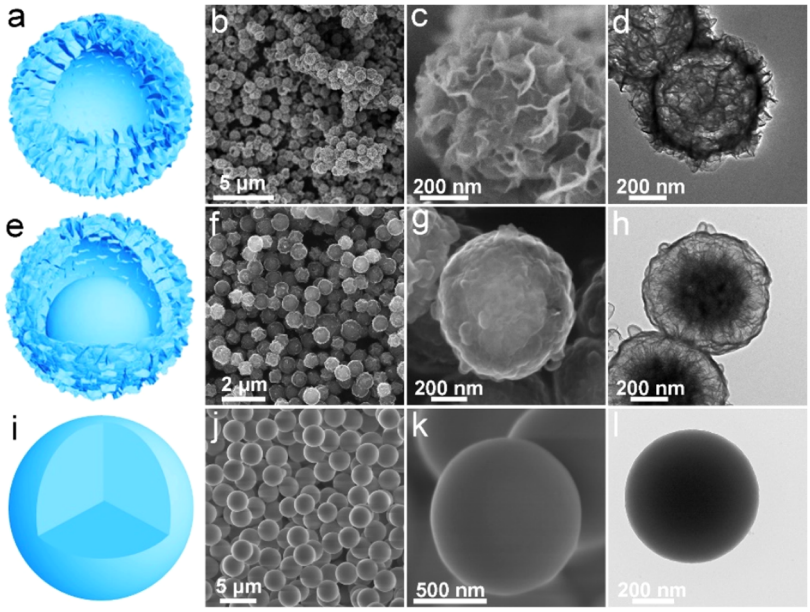

Figure 1. Structural models of H-MoS_2 (a), Y-MoS_2 (e), and S-MoS_2 (i). (b, c) SEM images and (d) TEM images of H-MoS_2. (f, g) SEM images and (h) TEM image of Y-MoS_2. (j, k) SEM images and (l) TEM image of S-MoS_2.

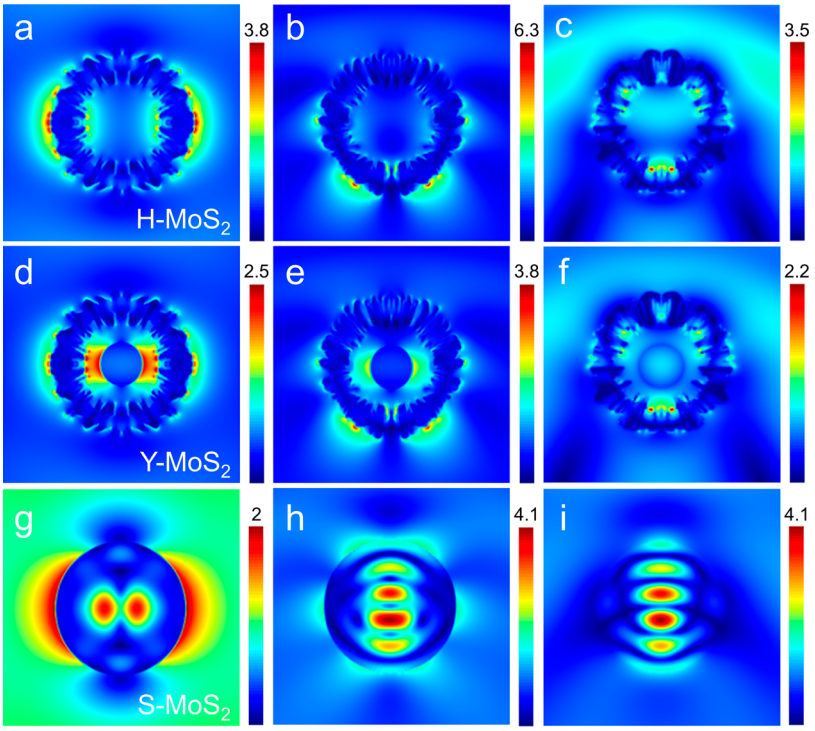

Figure 2. Corresponding simulated electric field distributions (808 nm) of S-MoS_2, H-MoS_2, and Y-MoS_2 resulted from FDTD simulations. (a−c) Distribution of electric field around H-MoS_2. (d−f) Distribution of electric field around Y-MoS_2. (g−i) Distribution of electric field around S-MoS_2. The electric fields from left to right are distributed along the $x-y$, $x-y$, and $y-z$ planes at the center of the sample, respectively.

dose of 366.97 J/cm^2 for 15 min, conducted twice a day. Within 24 h after irradiation, all experimental rats were euthanized and blood and tissue samples were collected for testing. Biochemical indicators testing was conducted on collected blood samples. The collected pancreatic tissue samples were fixed with 4% paraformaldehyde for 1 h and then embedded in paraffin. Next, the sample was cut into sagittal slices of thickness 4 μm and stained with hematoxylin and eosin (H&E). Finally, the obtained pathological sections were scored and photographed for observation.

3. RESULTS AND DISCUSSION

As shown in Scheme 1, H-MoS_2, Y-MoS_2, and S-MoS_2 were prepared by a hydrothermal method of sodium molybdate in a mixed solution of thiourea providing the sulfur source (Figure S1). The structural models of H-MoS_2, Y-MoS_2, and S-MoS_2 are shown in Figure 1a,e,i. Scanning electron microscopy (SEM) images show that H-MoS_2 exhibits a bridal bouquet-like morphology (Figures 1b,c and S2). Compared to H-MoS_2, Y-MoS_2 and S-MoS_2 have smoother surfaces (Figures 1f,g,j,k, S5,

https://doi.org/10.1021/acsanm.4c04712
ACS Appl. Nano Mater. 2025, 8, 3272−3280

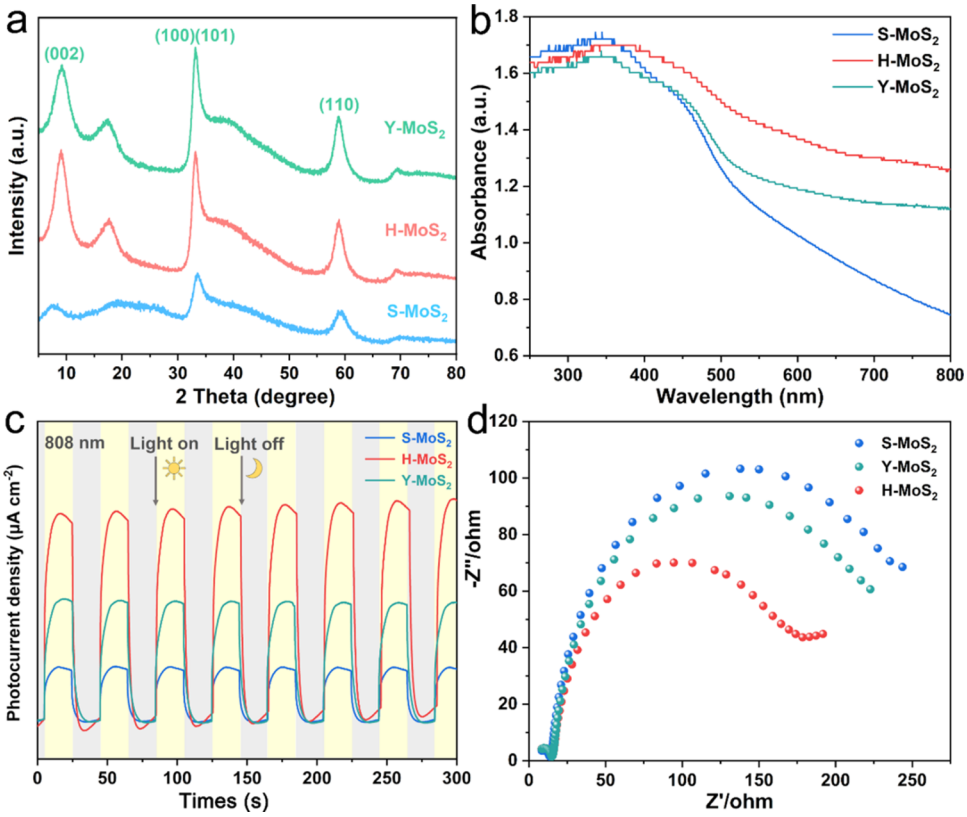

Figure 3. (a) XRD pattern, (b) UV−vis spectra, (c) photocurrent response, and (d) EIS of the S-MoS_2, H-MoS_2, and Y-MoS_2.

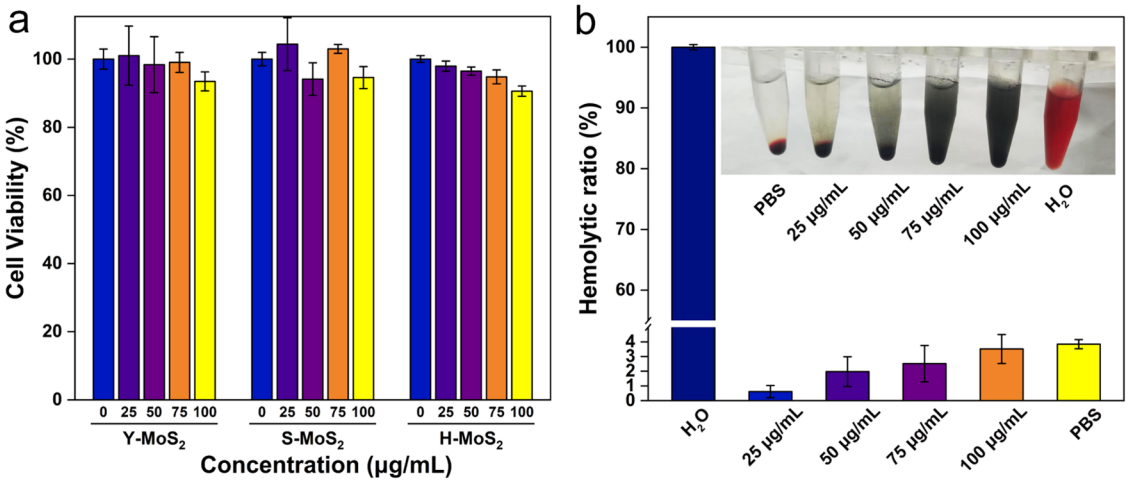

Figure 4. Safety of MoS_2 in vivo. (a) Cell viability of L929 after cultured with different concentrations of S-MoS_2, Y-MoS_2, and H-MoS_2. (b) Hemolysis ratio of red blood cells incubated with MoS_2 and photographs of red blood cells after centrifugation in the set.

and S7). Transmission electron microscopy (TEM) images reveal that H-MoS_2 is hollow inside while Y-MoS_2 has a solid sphere inside that has a gap with the outer wall. The S-MoS_2 is a solid sphere (Figures 1d,h,i, S4, S6, and S8). Energy-dispersive spectrometry (EDS) mapping shows that Mo, S, and C elements were uniformly distributed in the MoS_2 (Figure S3).

The intensity of the local electric field is directly related to the light absorption efficiency of the molecule, and the enhancement of the electric field helps to improve the catalytic effect.[29−31] Figure 2 studies the simulation results of electromagnetic field distributions for different light absorption nanoreactors. We employ the finite-difference time-domain (FDTD) to calculate the $x-y$, $x-z$, and $y-z$ electric field distribution of three nanoreactors. The results indicate that H-MoS_2 has a stronger electric field than Y-MoS_2 and S-MoS_2. The strong electric field is located in the sphere for S-MoS_2, which cannot be used well during light absorption, resulting in the light absorption being weakened. The electric field of Y-MoS_2 is mainly distributed in the gap between the solid core inside and the shell, forming a gap model that reduces light absorption. The electric field of H-MoS_2 is distributed outside the sphere, with its surface lamellar, thus giving H-MoS_2 a high light absorption and an enhanced electric field, so the photocatalytic activity of H-MoS_2 is the highest, which is conducive to the generation of ROS, to achieve the effect of treating SAP.

https://doi.org/10.1021/acsanm.4c04712
ACS Appl. Nano Mater. 2025, 8, 3272−3280

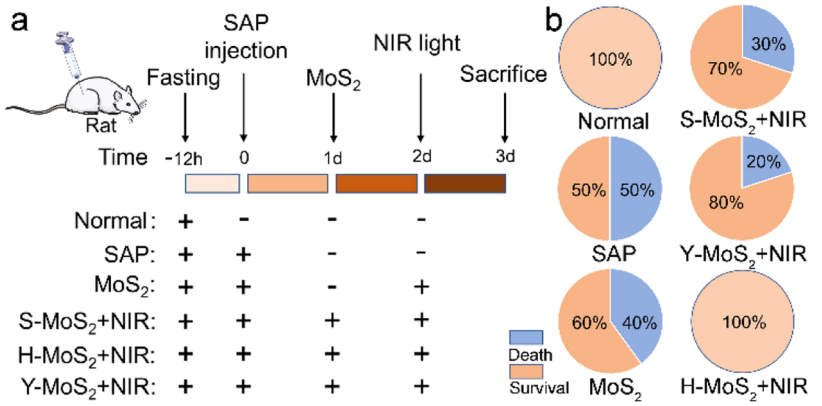

Figure 5. MoS_2 treatment alleviated the SAP. (a) Experimental scheme. (b) Fatality rate of the normal mice, SAP mice, and SAP mice treated with MoS_2, S-MoS_2+NIR, Y-MoS_2+NIR, and H-MoS_2+NIR.

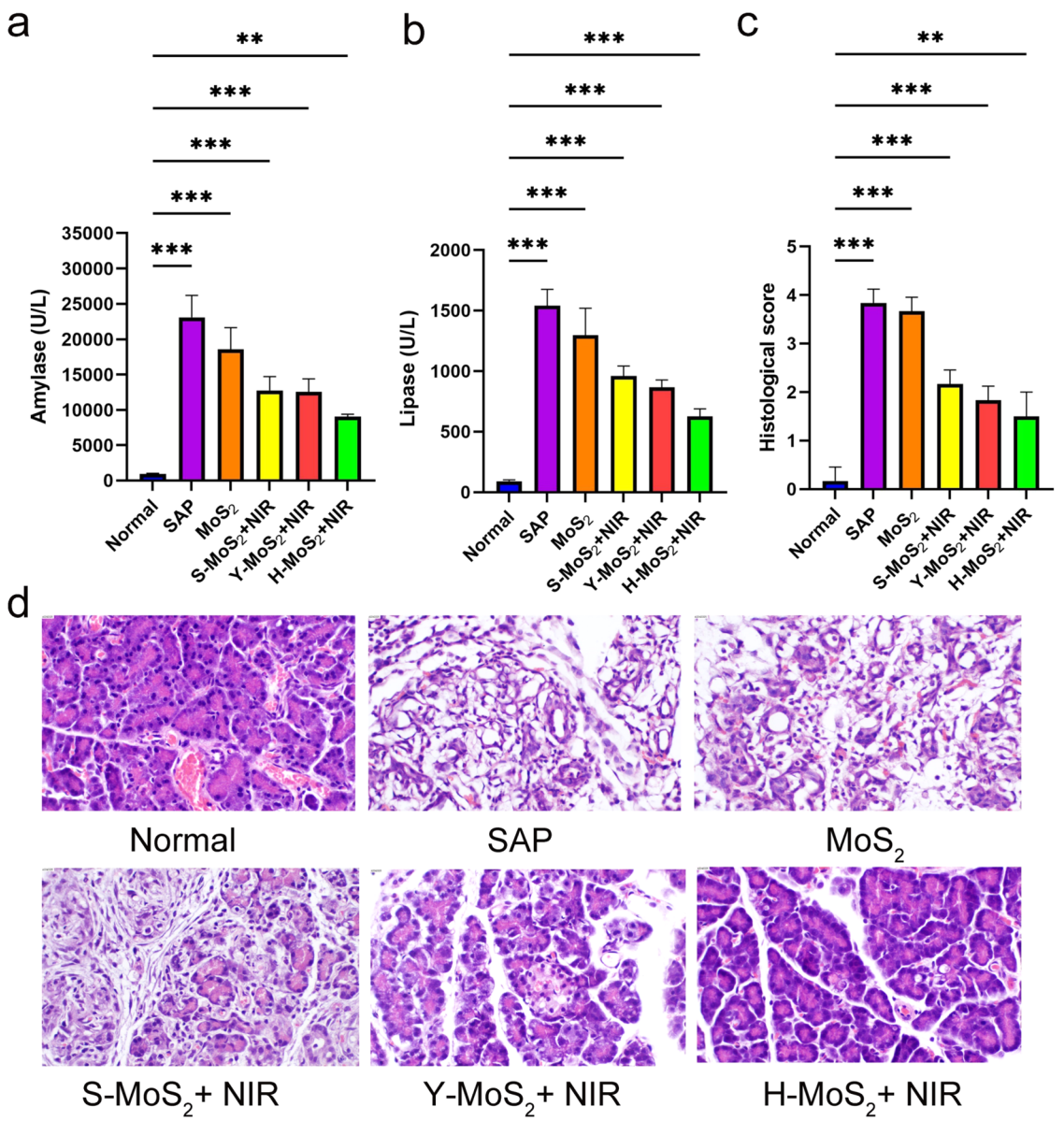

Figure 6. MoS_2 treatment alleviated the SAP. (a, b) Serum amylase and lipase levels at the end point of the experiment. (c) Histological score of pancreatic. (d) Representative H&E staining of pancreatic sections at the end point of the experiment.

https://doi.org/10.1021/acsanm.4c04712
ACS Appl. Nano Mater. 2025, 8, 3272−3280

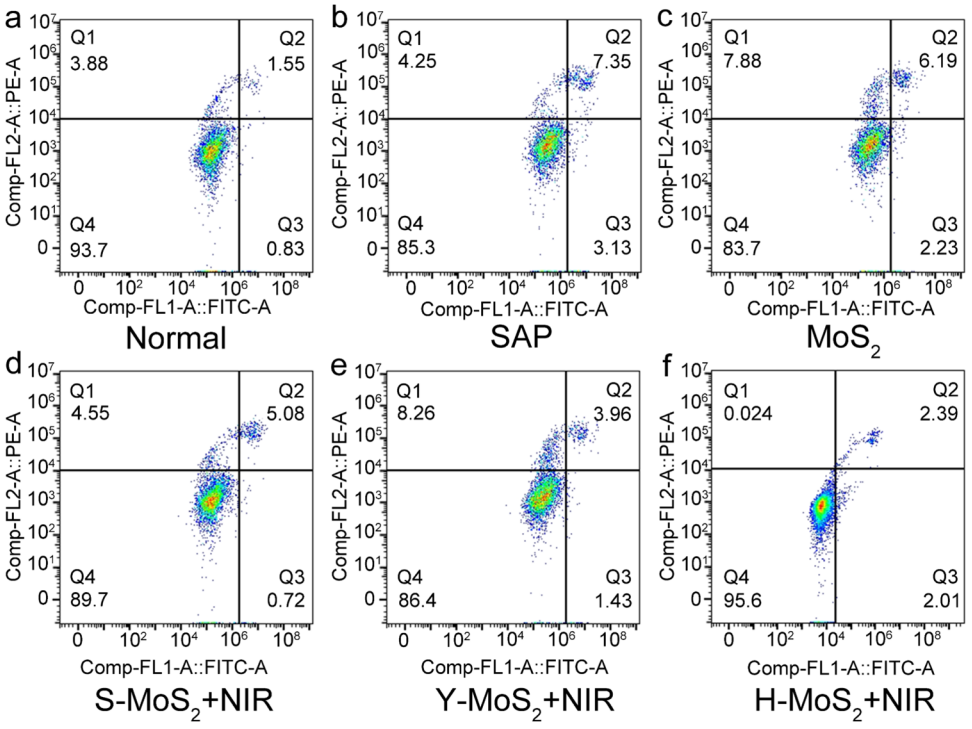

Figure 7. Cell apoptosis and necrosis distribution in the normal (a), SAP (b), and SAP treated with MoS_2 (c), S-MoS_2+NIR (d), Y-MoS_2+NIR (e), and H-MoS_2+NIR cells (f).

X-ray diffraction (XRD) patterns in Figure 3a show that all of the diffraction peaks correspond well to MoS_2. The peaks located at 8.78, 33.15, and 58.9° correspond to (002), (100), (101), and (110) of 2H-MoS_2, indicating that the morphology does not affect the crystal structure of MoS_2. There is no obvious difference among three MoS_2 nanoreactors in Raman peaks (Figure S9) and Fourier transform infrared spectroscopy (FT-IR) (Figure S10). The UV−vis spectra shown in Figure 3b demonstrate that H-MoS_2 has a wider adsorption range than Y-MoS_2, and S-MoS_2, which is consistent with the FDTD results above. The chemical states of H-MoS_2 are checked by X-ray photoelectron spectroscopy (XPS). In the high-resolution S 2p spectrum of H-MoS_2, two peaks at 162.1 and 163.3 eV belong to S $2p_{3/2}$ and S $2p_{1/2}$ of S species, respectively (Figure S11). Furthermore, the specific surface areas are 30.855, 16.331, and 6.6515 $m^2\ g^{-1}$ for H-MoS_2, Y-MoS_2, and S-MoS_2, respectively (Figure S12).

The photocurrent−time curves of H-MoS_2, Y-MoS_2, and S-MoS_2 were recorded through the light turning up/off process of the chronoamperometry method in Figure 3c. The H-MoS_2 has a higher photocurrent density than Y-MoS_2, and S-MoS_2, demonstrating an effective separation of photogenerated electron−hole pairs. Electrochemical impedance spectroscopy (EIS) (Figure 3d) was conducted to measure the charge-transfer resistance (R_{ct}) across the electrolyte/semiconductor interface. The semicircle of H-MoS_2 was smaller than those of Y-MoS_2, and S-MoS_2, implying a lower charge-transfer resistance. As stated thus, H-MoS_2 exhibits excellent superiority in charge separation and transfer.

As shown in Figure 4a, the activity of cells treated with different concentrations was almost unaffected, indicating the noncytotoxicity of MoS_2. Moreover, to further investigate the blood compatibility of MoS_2, we incubated Sprague−Dawley (SD) rat red blood cells for 2 h and removed the supernatant for absorbance detection. Figure 4b shows that almost all red blood cells in the ultrapure water group were ruptured with a hemolysis rate of 100%. However, when phosphate-buffered saline (PBS) solution and different concentrations of MoS_2 were added, red blood cell rupture was relatively rare, and the hemolysis rate was generally below 5%. This result indicates that MoS_2 will not cause damage to red blood cells.

Considering the above results, we chose a MoS_2 concentration of 100 μg/mL for subsequent experimental operation. As shown in Figure 5b, after successful induction of the SAP model in 3 days, the mortality rate of untreated rats was as high as 50%, while the mortality rate of SAP treated with MoS_2 alone was more than half. On the contrary, SAP rats induced by MoS_2 under NIR have a higher survival rate. The survival rates of rats using S-MoS_2 and Y-MoS_2 were not significantly different, but both were higher than those without NIR, while the survival rate of H-MoS_2 under NIR was the highest among others, reaching 100%.

Amylase and lipase are the two most used indicators in clinical practice to evaluate the efficacy of pancreatitis. Laboratory examination of acute pancreatitis showed elevated serum amylase and lipase levels, and the specificity of lipase elevation in the diagnosis of acute pancreatitis was better than that of amylase. As shown in Figure 6a,b, compared with the normal, the levels of amylase and lipase in the blood of SAP rats were absolutely increased, and the levels of amylase and lipase in the blood using MoS_2 alone were also higher than those of the normal. On the contrary, the levels of amylase and lipase in the blood of the MoS_2 under NIR remained relatively low, slightly higher than the normal, but lower than the SAP. In addition, when different forms of MoS_2 were used, the amylase and lipase levels of H-MoS_2 under NIR were significantly lower than those of S-MoS_2 and Y-MoS_2 under NIR, and both amylase and lipase levels were reduced to 1/3 of those of SAP. The results show that H-MoS_2 had excellent phototherapy effect on SAP.

https://doi.org/10.1021/acsanm.4c04712
ACS Appl. Nano Mater. 2025, 8, 3272−3280

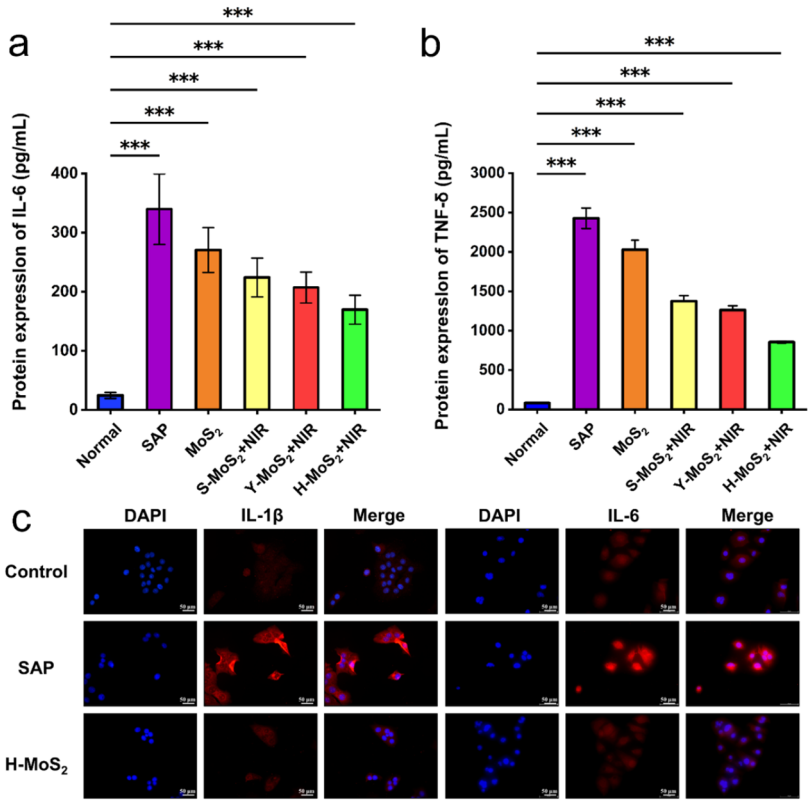

Figure 8. (a, b) Inflammatory marker analysis to measure the levels of IL-6 and TNF-α. (c) IL-1β and IL-6 staining detection of the effects of three different treatments on pancreatic acinar cell proliferation.

We further evaluated the efficacy of obtaining H&E staining for pancreatic tissue. As shown in Figure 6d, a large number of inflammatory cells such as neutrophils were observed in the pancreatic tissue of SAP rats, with significant tissue edema and accompanied by a certain degree of bleeding and necrosis compared to the normal rat pancreatic tissue. The original structure of the pancreatic lobes was observed in the pancreatic tissue of rats treated with MoS_2 under NIR, without significant tissue edema and necrosis. The pancreatic tissue morphology was intact, with H-MoS_2 under NIR being the closest to the normal. Using MoS_2 alone has more severe pancreatic tissue damage, similar to the SAP. At the same time, to better evaluate the damage to pancreatic tissue, we quantitatively scored inflammation, edema, bleeding, and necrosis in the tissue (Figure 6c). Compared with the normal, it can be seen that SAP has the highest score, indicating the most severe damage to pancreatic tissue. Using MoS_2 alone has the same score as the SAP, and the damage was also more severe. The score of the MoS_2 under NIR was slightly higher than that of the normal, but significantly lower than that of the SAP. It was found that in terms of pancreatic pathological evaluation, the treatment effect of the H-MoS_2 was better than that of the S-MoS_2 and Y-MoS_2 under NIR.

In addition, we explore the mechanism of photodynamic therapy for SAP. Through flow cytometry analysis, the apoptosis rate of pancreatic acinar cells in all groups was significantly reduced under NIR (Figure 7). This was because electrons in the MoS_2 band jumped into the conduction band under light, resulting in the separation of electron holes and the formation of electron-rich reducing end and hole-rich oxidizing end, and ROS was generated through oxidation−reduction reaction to inhibit the apoptosis of pancreatic cells. Among them, H-MoS_2 has the most significant therapeutic effect under NIR, which is basically close to the apoptosis rate of normal cells (Figure S13). Meanwhile, the result of Inflammatory marker analysis to measure the levels of IL-6 and TNF-α is that H-MoS_2 under NIR had the lowest IL-6 and TNF protein expression levels, which were close to normal (Figure 8a,b). Furthermore, IL-1β and IL-6 staining detection revealed that H-MoS_2 under NIR had an inhibitory effect on the secretion of inflammatory factors in pancreatitis (Figure 8c). The electron paramagnetic resonance (EPR) was used to detect the presence of free radicals, and 5,5-dimethyl-1-pyrroline (DMPO) was used as a spin capture reagent; $^{\bullet}O_2^-$ and $^{\bullet}OH$ radicals can be captured. As shown in Figure S13, there is a clear signal of $^{\bullet}O_2^-$, while the signal of $^{\bullet}OH$ is weak, indicating that $^{\bullet}O_2^-$ inhibits the apoptosis of pancreatic acinar cells (Figures S14 and S15).

4. CONCLUSIONS

We designed three morphologically controlled MoS_2 nanoreactors for SAP photodynamic therapy. In vitro biocompatibility studies show that MoS_2 nanoreactors have high safety and biocompatibility. In vivo experiments in rats verified that H-MoS_2 has a good therapeutic effect on SAP compared to that of S-MoS_2 and Y-MoS_2 nanoparticles under NIR excitation at a wavelength of 808 nm. This could be due to the production of $^{\bullet}O_2^-$ by MoS_2 under NIR, which reduces pancreatic cell apoptosis and thus has therapeutic effects. However, the specific functional formulations still need further research and proof from us. This work opened up a new path for constructing high-performance nanomaterials for the photodynamic therapy of SAP, especially in inflammation diseases.

https://doi.org/10.1021/acsanm.4c04712
ACS Appl. Nano Mater. 2025, 8, 3272−3280

■ ASSOCIATED CONTENT

Supporting Information

The Supporting Information is available free of charge at https://pubs.acs.org/doi/10.1021/acsanm.4c04712.

SEM images and the corresponding SEM mapping, TEM images and HRTEM images, Raman spectra, FT-IR spectra, XPS spectra, specific surface areas, and average pore diameter, safety of MoS_2 in vitro, MoS_2 treatment alleviated SAP, representative H&E staining of pancreatic sections at the end point, comparison of apoptosis and necrosis rates, electron paramagnetic resonance, and schematic illustration of a proposed mechanism on MoS_2 photocatalytic therapy (PDF)

■ AUTHOR INFORMATION

Corresponding Author

Sheng Ye − *Agricultural Photocatalysis Laboratory, School of Materials and Chemistry & College of Veterinary Medicine, Anhui Agricultural University, Hefei, Anhui 230036, P. R. China;* orcid.org/0000-0003-2314-2856; Email: sye503@ahau.edu.cn

Authors

Ruixi Chu − *Agricultural Photocatalysis Laboratory, School of Materials and Chemistry & College of Veterinary Medicine, Anhui Agricultural University, Hefei, Anhui 230036, P. R. China*

Yuansong Sun − *Department of Emergency Surgery & Research Center of Minimally Invasive Intervention, The Second Affiliated Hospital of Anhui Medical University, Hefei, Anhui 230001, P. R. China*

Jianhua Liu − *Department of Critical Care Medicine, The Affiliated Chuzhou Hospital of Anhui Medical University (The First People's Hospital of Chuzhou), Chuzhou, Anhui 239000, P. R. China*

Yibin Du − *Department of Spinal Orthopaedics, The Third Affiliated Hospital of Anhui Medical University (The First People's Hospital of Hefei), Hefei, Anhui 230061, P. R. China*

Weihong Chen − *Department of Emergency Surgery & Research Center of Minimally Invasive Intervention, The Second Affiliated Hospital of Anhui Medical University, Hefei, Anhui 230001, P. R. China*

Rongrong Gu − *Agricultural Photocatalysis Laboratory, School of Materials and Chemistry & College of Veterinary Medicine, Anhui Agricultural University, Hefei, Anhui 230036, P. R. China*

Complete contact information is available at: https://pubs.acs.org/10.1021/acsanm.4c04712

Author Contributions

⊥R.C., Y.S., J.L., Y.D., and W.C. contributed equally. R.C., Y.S., J.L., Y.D., and W.C.: investigation, experimentation, data curation, formal analysis, writing—original draft. R.G.: software, supervision, validation, visualization. S.Y.: conceptualization, resources, methodology, project administration, writing—review and editing.

Notes

The authors declare no competing financial interest.

■ ACKNOWLEDGMENTS

This work was financially supported by National Natural Science Foundation of China (22372001), Anhui Natural Science Foundation for Outstanding Young Scholars (2408085Y008), Starting Fund for Scientific Research of High-Level Talents, Anhui Agricultural University (rc382108), Innovation and entrepreneurship training program for college students, Anhui Agricultural University (X202410364241), Anhui Provincial Health Research Program (AHWJ2022b113), Basic and Clinical Collaboration Program of Anhui Medical University (2022sfy004), and the 2024 Research Project of the Chuzhou Municipal Health and Health Commission (CZWJ2024C003). The authors thank Dr. Qin Wang and Dr. Yang Xu from the Biotechnology Center of Anhui Agricultural University for their help with catalyst characterization in this work.

■ REFERENCES

(1) Xiao, A. Y.; Tan, M. L. Y.; Wu, L. M.; Asrani, V. M.; Windsor, J. A.; Yadav, D.; Petrov, M. S. Global incidence and mortality of pancreatic diseases: a systematic review, meta-analysis, and meta-regression of population-based cohort studies. *Lancet Gastroenterol. Hepatol.* **2016**, *1* (1), 45−55.

(2) Wang, Y.; Li, Y.; Gao, S.; Yu, X.; Chen, Y.; Lin, Y. Tetrahedral framework nucleic acids can alleviate taurocholate-induced severe acute pancreatitis and its subsequent multiorgan injury in mice. *Nano Lett.* **2022**, *22* (4), 1759−1768.

(3) Mederos, M. A.; Reber, H. A.; Girgis, M. D. Acute pancreatitis. *Jama* **2021**, *325* (4), 382−390.

(4) van Dijk, S. M.; Hallensleben, N. D. L.; van Santvoort, H. C.; Fockens, P.; van Goor, H.; Bruno, M. J.; Besselink, M. G. Acute pancreatitis: recent advances through randomised trials. *Gut* **2017**, *66* (11), 2024−2032.

(5) Trikudanathan, G.; Wolbrink, D. R. J.; van Santvoort, H. C.; Mallery, S.; Freeman, M.; Besselink, M. G. Current concepts in severe acute and necrotizing pancreatitis: an evidence-based approach. *Gastroenterology* **2019**, *156* (7), 1994−2007.

(6) Johnson, C. D. Persistent organ failure during the first week as a marker of fatal outcome in acute pancreatitis. *Gut* **2004**, *53* (9), 1340−1344.

(7) Schepers, N. J.; Bakker, O. J.; Besselink, M. G.; Ali, U. A.; Bollen, T. L.; Gooszen, H. G.; van Santvoort, H. C.; Bruno, M. J. Impact of characteristics of organ failure and infected necrosis on mortality in necrotising pancreatitis. *Gut* **2019**, *68* (6), 1044−1051.

(8) Garg, P. K.; Singh, V. P. Organ failure due to Systemic injury in acute pancreatitis. *Gastroenterology* **2019**, *156* (7), 2008−2023.

(9) Xie, X.; Zhao, J.; Gao, W.; Chen, J.; Hu, B.; Cai, X.; Zheng, Y. Prussian blue nanozyme-mediated nanoscavenger ameliorates acute pancreatitis via inhibiting TLRs/NF-κB signaling pathway. *Theranostics* **2021**, *11* (7), 3213−3228.

(10) Liu, T.; Wang, C.; Cui, W.; Gong, H.; Liang, C.; Shi, X.; Li, Z.; Sun, B.; Liu, Z. Combined photothermal and photodynamic therapy delivered by PEGylated MoS_2 nanosheets. *Nanoscale* **2014**, *6* (19), 11219−11225.

(11) Chen, J.; Fan, T.; Xie, Z.; Zeng, Q.; Xue, P.; Zheng, T.; Chen, Y.; Luo, X.; Zhang, H. Advances in nanomaterials for photodynamic therapy applications: Status and challenges. *Biomaterials* **2020**, *237*, 119827−119854.

(12) Dong, M.; Tang, R.; Li, J.; Zhao, J.; Wang, Y.; Ouyang, L.; Lu, W.; Tao, J.; Dang, M.; Tang, Y.; Teng, Z. Mitochondria-targeted Janus mesoporous nanoplatform for tumor photodynamic therapy. *Chin. Chem. Lett.* **2024**, *35* (2), 108539−108543.

(13) Huang, X.-Y.; Hu, D.-W.; Zhao, F.-J.; Verbruggen, N. Molybdenum: More than an essential element. *J. Exp. Bot.* **2022**, *73* (6), 1766−1774.

(14) Novotny, J. A.; Peterson, C. A. Molybdenum. *Adv. Nutr.* **2018**, *9* (3), 272−273.

(15) Ye, S.; Ding, C.; Liu, M.; Wang, A.; Huang, Q.; Li, C. Water oxidation catalysts for artificial photosynthesis. *Adv. Mater.* **2019**, *31* (50), No. 19002069.

(16) Gong, F.; Liu, M.; Gong, L.; Ye, S.; Jiang, Q.; Zeng, G.; Zhang, X.; Peng, Z.; Zhang, Y.; Fang, S.; et al. Modulation of Mo−Fe−C sites over

mesoscale diffusion-enhanced hollow sub-micro reactors toward boosted electrochemical water oxidation. *Adv. Funct. Mater.* **2022**, *32* (30), No. 2202141.
(17) Wang, L.; Zhang, C.; Cao, Z.; Zeng, G.; Liu, J.; Ye, S. Dual modulation of bulk electronic structure and surficial active sites in sea urchin-like MoO_2 nanoreactors promoting electrocatalytic hydrogen evolution. *Adv. Funct. Mater.* **2024**, *34* (42), No. 2406670.
(18) Dhas, N.; Kudarha, R.; Garkal, A.; Ghate, V.; Sharma, S.; Panzade, P.; Khot, S.; Chaudhari, P.; Singh, A.; Paryani, M.; et al. Molybdenum-based hetero-nanocomposites for cancer therapy, diagnosis and biosensing application: current advancement and future breakthroughs. *J. Controlled Release* **2021**, *330*, 257−283.
(19) Chen, L.; Feng, Y.; Zhou, X.; Zhang, Q.; Nie, W.; Wang, W.; Zhang, Y.; He, C. One-pot synthesis of MoS_2 nanoflakes with desirable degradability for photothermal cancer therapy. *ACS Appl. Mater. Interfaces* **2017**, *9* (20), 17347−17358.
(20) Yadav, V.; Roy, S.; Singh, P.; Khan, Z.; Jaiswal, A. 2D MoS_2-based nanomaterials for therapeutic, bioimaging, and biosensing applications. *Small* **2019**, *15* (1), 1803706−1803739.
(21) Gong, F.; Liu, M.; Gong, L.; Ye, S.; Jiang, Q.; Zeng, G.; Zhang, X.; Peng, Z.; Zhang, Y.; Fang, S.; Liu, J. Modulation of Mo−Fe−C sites over mesoscale diffusion-enhanced hollow sub-micro reactors toward boosted electrochemical water oxidation. *Adv. Funct. Mater.* **2022**, *32* (30), 2202141−2202153.
(22) Liu, M.; Zhu, J.; Liu, Y.; Gong, F.; Li, R.; Chen, H.; Zhao, M.; Jiang, Q.; Liu, J.; Ye, S. Modulating the electronic structures of layer-expanded MoS_2 nanoreactor via cobalt doping and carbon intercalation for enhanced electrocatalytic hydrogen evolution. *Chem. Eng. J.* **2022**, *446*, 137080−137089.
(23) Park, M.; Park, Y. J.; Chen, X.; Park, Y. K.; Kim, M. S.; Ahn, J. H. MoS_2-based tactile sensor for electronic skin applications. *Adv. Mater.* **2016**, *28* (13), 2556−2562.
(24) Chen, Q.; Liu, Z. Albumin carriers for cancer theranostics: a conventional platform with new promise. *Adv. Mater.* **2016**, *28* (47), 10557−10566.
(25) Jiang, F.; Ding, B.; Liang, S.; Zhao, Y.; Cheng, Z.; Xing, B.; Ma, P.; Lin, J. Intelligent MoS_2−CuO heterostructures with multiplexed imaging and remarkably enhanced antitumor efficacy via synergetic photothermal therapy/ chemodynamic therapy/ immunotherapy. *Biomaterials* **2021**, *268*, 120545−120557.
(26) Kapri, S.; Bhattacharyya, S. Molybdenum sulfide−reduced graphene oxide p−n heterojunction nanosheets with anchored oxygen generating manganese dioxide nanoparticles for enhanced photodynamic therapy. *Chem. Sci.* **2018**, *9* (48), 8982−8989.
(27) Hu, X.; Xia, F.; Lee, J.; Li, F.; Lu, X.; Zhuo, X.; Nie, G.; Ling, D. Tailor-made nanomaterials for diagnosis and therapy of pancreatic ductal adenocarcinoma. *Adv. Sci.* **2021**, *8* (7), 2202545−2002592.
(28) Zhang, Z.; Wang, L.; Liu, W.; Yan, Z.; Zhu, Y.; Zhou, S.; Guan, S. Photogenerated-hole-induced rapid elimination of solid tumors by the supramolecular porphyrin photocatalyst. *Natl. Sci. Rev.* **2021**, *8* (5), 155−164.
(29) Lee, H. Y.; Yi, S. N. FDTD simulation of local electric field enhancement caused by nanoscale roughness comprising of different metals under the solar spectrum. *J. Korean Phys. Soc.* **2023**, *82* (11), 1078−1083.
(30) Awazu, K.; Fujimaki, M.; Rockstuhl, C.; Tominaga, J.; Murakami, H.; Ohki, Y.; Yoshida, N.; Watanabe, T. A plasmonic photocatalyst consisting of silver nanoparticles embedded in titanium dioxide. *J. Am. Chem. Soc.* **2008**, *130*, 1676−1680.
(31) Wang, H.-L.; You, E.-M.; Panneerselvam, R.; Ding, S.-Y.; Tian, Z.-Q. Advances of surface-enhanced Raman and IR spectroscopies: from nano/microstructures to macro-optical design. *Light: Sci. Appl.* **2021**, *10* (1), 161−180.

https://doi.org/10.1021/acsanm.4c04712
ACS Appl. Nano Mater. 2025, 8, 3272−3280